VALIDATION OF CIRA FLOW SOLVER ZEN FOR SCT LOW-SPEED HIGH-LIFT COMPUTATIONS

Brandi, V., Amato, M., and Catalano, P.
CIRA - Italian Aerospace Research Center
Via Maiorise, 81043 Capua (CE), Italy

Keywords: *CFD, RANS, Supersonic Commercial Transport, High Lift*

Abstract

The objective of this paper is to validate the CIRA flow solver ZEN for the low speed performance computations of Supersonic Commercial Transport (SCT) high lift configuration. This work is set into the framework of the EU funded research project "EPISTLE", whose principal aim is to assess an aerodynamic methodology that shall allow to design SCT "new generation" with largely attached flows at low-speed high-lift conditions. This will lead to a considerable reduction of engine power in compliance with the next years Community regulations which will impose severe limits to engine noise and pollution. The industrial partners formulated accuracy requirements for the global aerodynamic coefficients to compare with an experimental database created during the EPISTLE program. Various angles of attack have been calculated to review the different flow field behaviour from full attached flow to the onset of separation phenomena. Grid dependency and turbulence models effect have been taken into account.

The CIRA flow solver ZEN has demonstrated the capability to capture the main aspects of separation phenomena on the SCT wing and to fulfil the accuracy requirements on the global aerodynamic coefficients.

1 Introduction

As part of WP2 program of the EU "EPISTLE" (European Project for the Improvement of Supersonic Transport Low speed Efficiency) project, the partners involved in the numerical prediction of high-lift low-speed Supersonic Commercial Transport (SCT) configuration performances had to demonstrate the capabilities of their codes to meet the industrial accuracy limit requirements on the aerodynamic coefficients and to compute the pressure distribution by detecting the main phenomenology at attached and separated flow conditions [5]. The numerical tests have been carried out on the so-called *"datum"* low-speed high-lift European SCT (ESCT) configuration [4], that was designed within the previous EU funded EUROSUP project only by approximate methods [8]. Indeed, during this project, an optimised supersonic (over sea) and transonic (over land) cruise configuration was found, and an extensive validation of the numerical tools was performed at transonic and supersonic conditions. An experimental database on the ESCT 1:80 model at low speed conditions was already created during the previous EUROSUP project [3, 10], and completed and updated during a new wind tunnel test campaign as part of WP1 of EPISTLE program at HST-DNW facility [11].

The objective of this work is to assess the capabilities of CIRA Navier-Stokes code, ZEN [7], to predict the main flow features on the
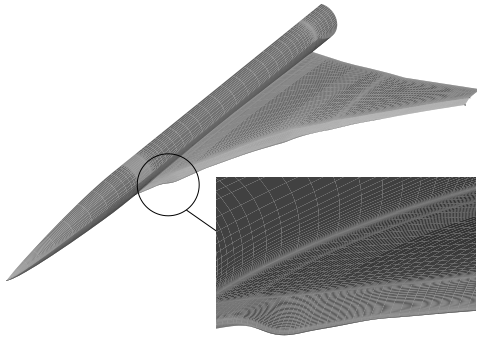
Fig. 1 Low-speed high-lift SCT configuration as designed during EUROSUP project
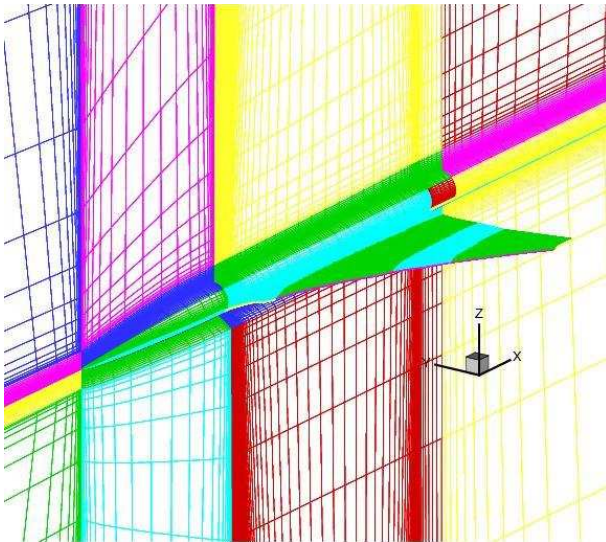

Fig. 2 Simmetry plane and surface point distribution of the CIRA grid

ESCT high-lift configuration.

2   Grid generation around the *"datum"* configuration

The EPISTLE *"datum"* configuration is shown in Figure 1; the nose droop leading edge on the optimised supersonic wing shape is well evident in the picture detail.

A mesh was initially generated on this configuration by the German Aerospace Research

Center (DLR) during the previous GARTEUR action group (AD) AG-30; an improved version with 793,892 cells within a C-O topology, was delivered to all partners at the beginning of EPISTLE project to perform code to code comparisons on a common mesh. The surface grid is representative of the 1:80 scale low-speed ESCT configuration with a cilindrical sting in the rearside of the fuselage section in order to reproduce the appropriate wind tunnel layout during the EPISTLE tests.

Since the results CIRA obtained on DLR grid were not satisfactory in terms of solution convergence, as it will be shown later on, CIRA has decided to generate a new grid. This grid has the same computational domain extension as the DLR (six semi-span in each directions) but with more cells into the streamwise and the spanwise directions in order to capture the main features of such flow. A C-C near-field topology embedded in a C far-field is employed; the total number of cells is 2,285,600 on the finer level.

Figure 2 shows a global view of simmetry plane and wing-fuselage surface point distribution of the CIRA grid.

3   Analysis of computational results

The computations have been performed at Mach number of 0.25 and with a Reynolds number of 7.3×10^6. These flow specifications reproduce the EPISTLE wind tunnel campaign. CIRA has applied the Reynolds Average Navier-Stokes (RANS) flow solver ZEN [7]. The flow equations are discretized by means of a cell centered finite volume scheme with blended self adaptive second and fourth order artificial dissipation. The solution procedure is based on a time marching concept. A multigrid scheme can be used to accelerate the convergence of the solution and performs relaxations, by using the Runge Kutta algorithm with local time stepping and residual averaging, on different grid levels. The turbulence equations are uncoupled by the RANS equations and are solved, inside a multigrid cycle,

only on the finest grid level.

Full turbulent flow conditions have been applied on the wing and on the fuselage. Indeed, during the wind tunnel tests, the partners recognised that there were not appreciable differences among the experimental coefficients with different transition trips layout and with free transition conditions [11]. Moreover, the boundary layer stability analysis performed by CIRA confirmed that the transition to turbulent flow occurred rapidly very close to the wing leading edge [1].

Four angles of attack have been tested: $6°$ for attached flow conditions, $8°$ for mainly attached flow, $9°$ for transient flow and $10°$ for mainly separated flow.

Most of the calculations have been performed with the Kok TNT $\kappa - \omega$ turbulence model (TM) [6, 2]; the Myong-Kasagi $\kappa - \epsilon$ TM [9] has been run for comparison only at $8°$. The multi-grid technique has been applied to evaluate the advantage in terms of convergence speed.

3.1 Flow solver convergence: comparison of numerical methods.

ZEN code showed poor convergence on the DLR common grid. Thus, a new mesh has been generated at CIRA. Figure 3 shows the convergence history on both grids at $6°$ with the $\kappa - \omega$ TM and with the same and non-optimised numerical parameters. The aerodynamic coefficient values in the convergence plots have been intentionally left out. However, for each AOA, the scales on the plots are the same in order to let the plots comparable. Figure 4 shows the comparison of convergence at $8°$ with the Kok TNT $\kappa - \omega$. Different CFL numbers and artificial viscosity levels have been used in order to judge their influence on the solution. Figure 5 shows at $8°$ the Myong-Kasagi $\kappa - \epsilon$ TM solution with and without the multigrid technique. The $\kappa - \omega$ TM solution converges more rapidly than the $\kappa - \epsilon$ one under the same numerical parameters and the converged C_L and C_D are comparable.

In order to get an increase of convergence rate, the $\kappa - \epsilon$ TM was also run with the multigrid technique. Figure 5 shows that a valuable increase of convergence rate is obtained for both residuals and lift.

At $6°$ and $8°$ both residuals and aerodynamic coefficients reach a steady state convergence level with a non-oscillatory behaviour; the iterations to reach steady state are increasing with the angle of attack. Figure 6 shows the convergence at $10°$ with the same non-optimised numerical parameters. Due to the strong vortex-vortex interaction on the wing, a steady state convergence level cannot be reached and both residuals and aerodynamic coefficients show low amplitude oscillations around a mean value. Here, for space shortage, the convergence rate at $9°$ with the $\kappa - \omega$ TM and multigrid technique has not been shown.

3.2 Aerodynamic coefficients

This section presents the comparison between the calculated and the measured global aerodynamic coefficient. The experimental data refer to the most effective transition strip layout during the EPISTLE wind tunnel tests, named *"fixed 3"*. This transition fixing, consisting of a continuous tripping bands on the upper and lower wing leading edge, assures turbulent flow conditions on the wing. Therefore, the full turbulent flow assumptions in the computations are justified. Only the results obtained on CIRA grid will be shown.

The lift curve is shown in Figure 7. The upper and lower bounds represent the requirements dictated by the industrial partners of the project. Although the required calculation accuracy has to be intended to be satisfied only at nominal attached flow conditions ($6°$ and $8°$), the plot shows that the results are well within the industrial requirements for all the tested incidences with both turbulence models.

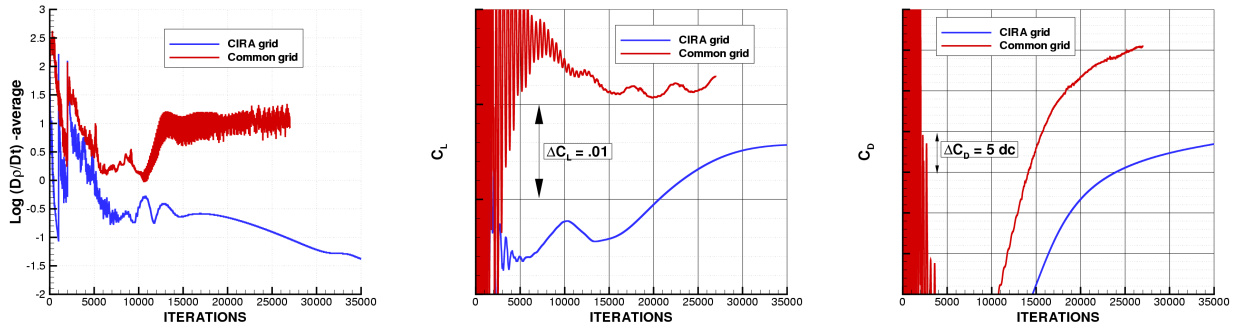The drag polar is shown in Figure 8. The flow solution at $6°$ is well within the accuracy

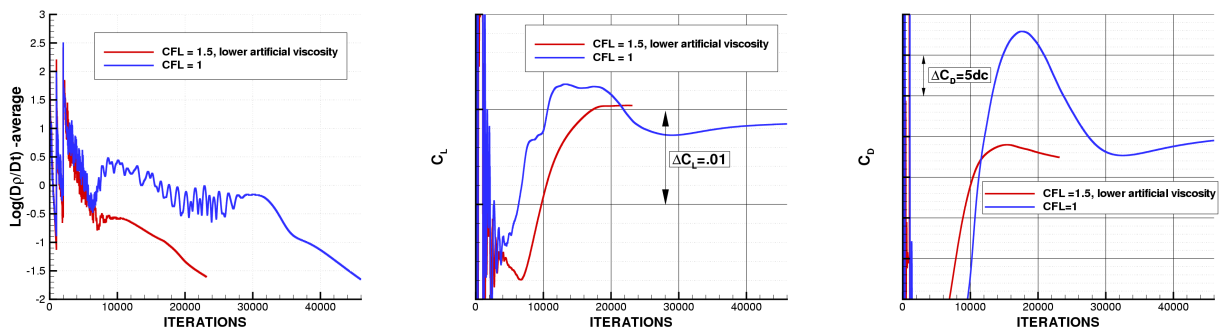**Fig. 3** Convergence on CIRA and common grid: Kok TNT $\kappa - \omega$ TM, $\alpha = 6°$

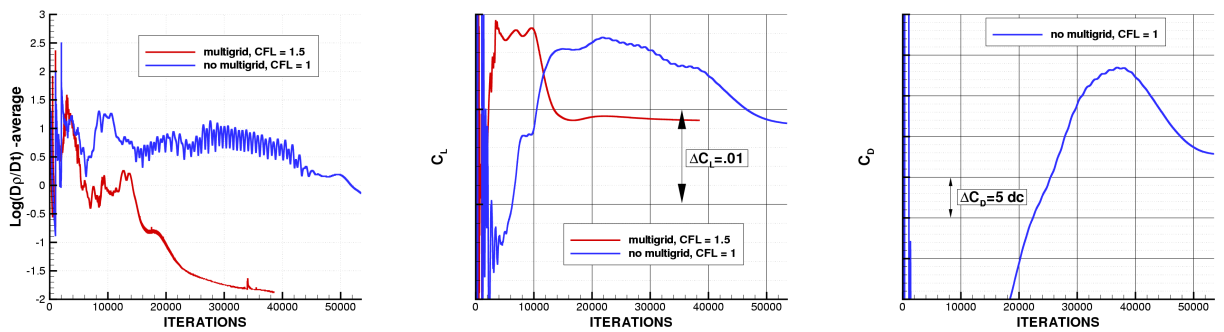**Fig. 4** Convergence on CIRA grid, Kok TNT $\kappa - \omega$ TM, $\alpha = 8°$

Fig. 5 Convergence on CIRA grid, Myong-Kasagi $\kappa - \epsilon$ TM, $\alpha = 8°$

band. The acceptance band is built here with the drag requirement of $\pm$ 17 drag counts at the same lift coefficient. By increasing the incidence the calculated points move toward the lower boundary of the accuracy area. Taking into account that accuracy requirements have been strictly defined for merely attached flows, the qualification for flows containing separation is somewhat less restrictive than indicated by the band itself. At 8°, both turbulence models give results just on the lower boundary limit.

The piching moment curve is reported in Figure 9. Here, the accuracy limits have been built by using the requirement on piching moment of $\pm$ .0035 at the same lift coefficient. The comparison between the measured and the calculated points is well within the accu-
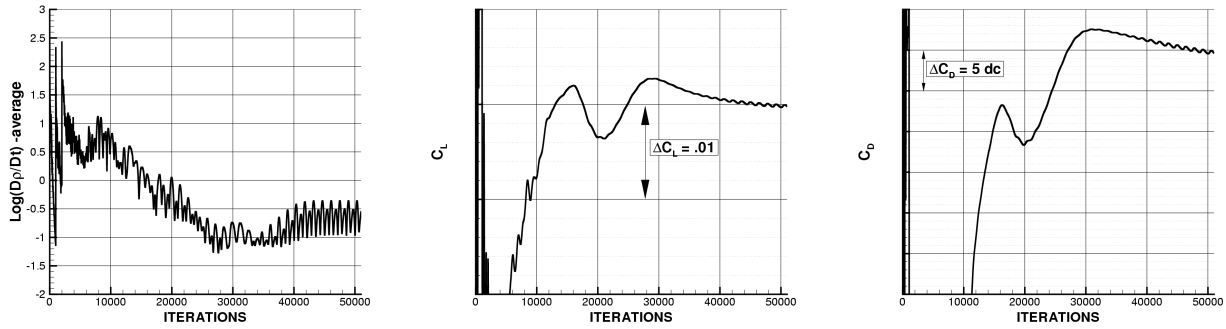
Fig. 6 Convergence on CIRA grid, Kok TNT $\kappa - \omega$ TM, $\alpha = 10°$

racy range also at the highest angles of attack. Moreover, the non linearity occurring at the onset of separation seems to be well captured by the CIRA code.
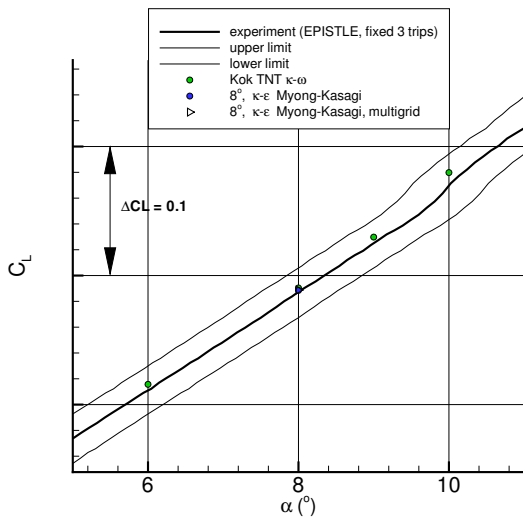

Fig. 7 Comparison of computed and measured lift curve

3.3 Pressure coefficients

Here, the experimental pressure coefficient data, produced during the previous EURO-SUP wind tunnel test campaign, have been used for comparison.

The pressure data were measured into three well-defined sections along the wing span, namely an inboard section, $\eta = .29$, a mid-span section at $\eta = .52$ and an outboard section at $\eta = .71$.
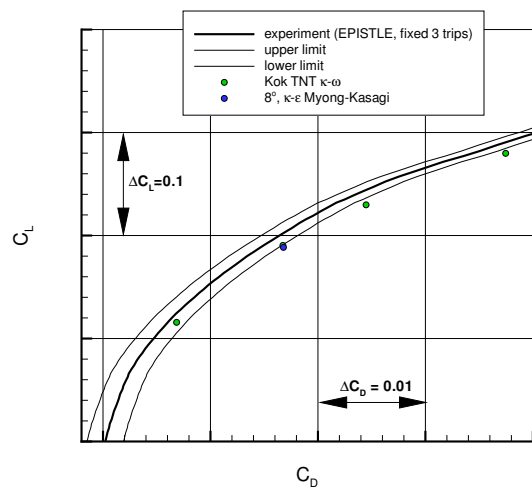

Fig. 8 Comparison of computed and measured drag polar

Pressure taps were put on the leeward and on the windward side except at mid-span where the measurements were made only on the leeward side.

The comparison between the calculated and the measured data is generally very good on the pressure side at all the considered incidences as can be easily observed in Figure 10 - 12.

At 6° when the flow is fully attached (Figure 10), the comparison between the calculated and the experimental data can be considered satisfatory especially in the two inner wing sections. In the outboard one the calculated pressure peak is overpredicted.
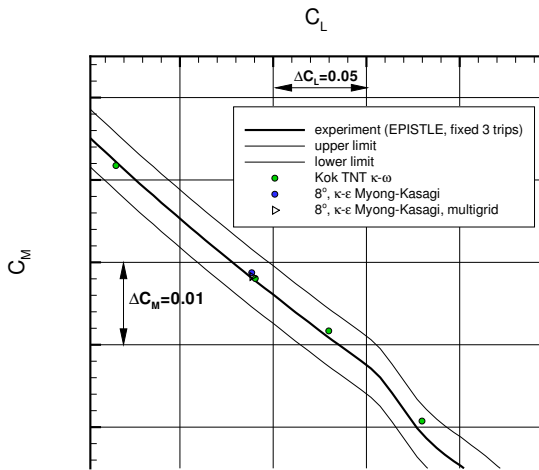
At 8° (Figure 11), the flow is mainly at-

Fig. 9 Comparison of computed and measured piching moment curve against lift

tached but some evidences of vortical structure appear in the experimental pressure distribution. In the inner and mid-span sections, the vortex flow downstream the hingeline is well predicted by both turbulence models. In the mid-span section the suction peak on the knuckle position is well captured while the flow separation on the nose-droop slat has been not well predicted. The outboard section highlights attached flow with good agreement between the computed data and the experimental one, although the knuckle suction peak is overpredicted by both turbulence models.

At 10° (Figure 12), separations occur all over the wing span and the regions of vortical flow found by the experiments sometimes mismatch with the computed one, especially on the outboard section. The results in the inboard section highlight that both the intensity and the location of vortex have been well predicted. The mismatching between the computed and the measured pressure level in the more outer sections accounts for the higher lift coefficient at this incidence with respect the experimental data. A more detailed discussion of vortex flow development on the wing is given in the next section.

3.4 Vortex flow development with the angle of attack

The results obtained during the additional EPISTLE wind tunnel test campaign have been exploited to detect the separation development phenomena on the wing and, thus, to further confirm the reliability of the numerical simulations. Here, the computed limiting surface streamlines are compared with the oil flow picture and the assumed flow topology from the oil flow interpretation [1] is compared with the calculated pressure losses on spanwise vertical plane over the wing in order to verify the vortex flow region extension.

Experimental oil flow visualisations were performed on the low-speed high-lift SCT configuration for three angles of attack, 6°, 8° (the upper side in Figure 13) and 10.5°, during the EPISTLE wind tunnel test campaign while during the EUROSUP wind tunnel test campaign oil flow visualisation was carried out at 10° [3] as shown on the left hand side of Figure 16.

The computed limiting streamlines at 6° are plotted on the left hand side of Figure 14 with the pressure distribution as background; the flow is fully attached on both side of the wing; the comparison between the oil flow picture and the upper side limiting streamline pattern is very good.

The computed limiting streamlines at 8° are shown on the right hand side of Figure 14. The flow is fully attached on the wing lower side. The comparison between the oil flow visualisation and the calculated limiting streamline pattern can be considered satisfactory at a glance; the growing kink vortex structure in the mid-span is well replicated by the numerical solution; on the contrary the inner vortex structure appears to be shifted outboard with respect the experimental data and it clearly shows the trend to merge more rapidly into the kink vortex. This behaviour is also confirmed by the pressure loss contour plot shown on the left hand side of Figure 15. The stub vortex seems to be not well captured; a more external
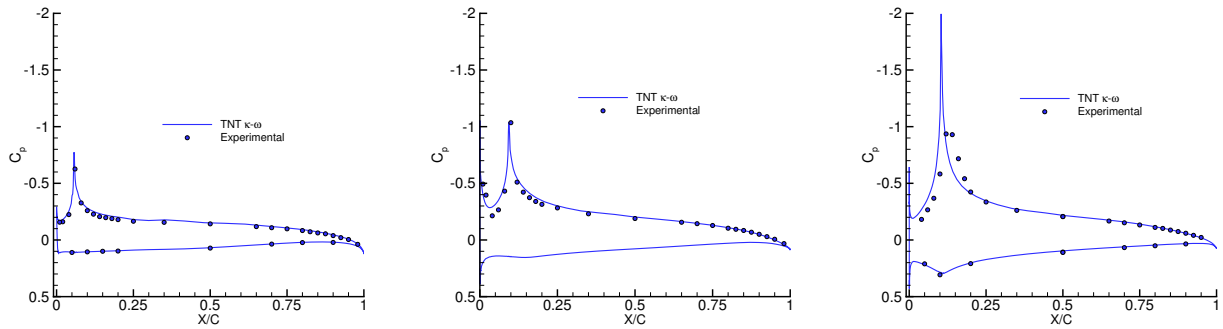
Fig. 10 Comparison of computed and measured pressure coefficient, $\alpha = 6°$, $\eta = .29$ (left), $\eta = .52$ (middle), $\eta = .71$ (right)
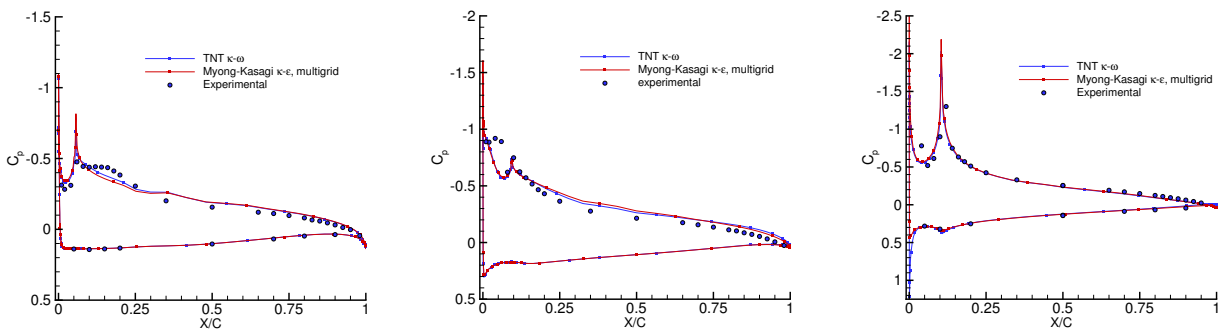

Fig. 11 Comparison of computed and measured pressure coefficient, $\alpha = 8°$, $\eta = .29$ (left), $\eta = .52$ (middle), $\eta = .71$ (right)
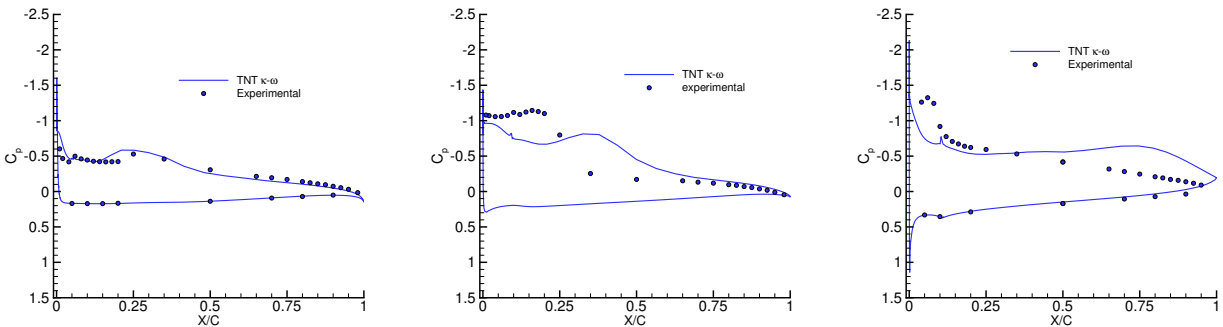

Fig. 12 Comparison of computed and measured pressure coefficient, $\alpha = 10°$, $\eta = .29$ (left), $\eta = .52$ (middle), $\eta = .71$ (right)

vortex is fed by the leading edge vorticity and it is swalloed up at about mid-span by the stronger kink vortex. The tip vortex structure is well evident too. By comparing the vortical structure drawn from the pressure loss contour plot and the one in the picture of Figure 17,

as assumed from the oil flow visualisations, the numerical prediction does not exactly replicate the inner vortex structure at the trailing edge position.

The calculated limiting streamlines at 10° and the oil flow visualisation are shown in Fig-

ure 16. In order to get a clearer interpretation, it is useful to have a look at the total pressure loss on the right hand side of Figure 15. Indeed, at this incidences the stub vortex is captured but it rapidly slips under an outboard vortex which is more evident in the skin friction line plot. The position of the core of this vortex is more shifted outboard with respect to the experimental data. This first vortex structure, then, will interact with the kink vortex structure which, at this incidence, is stronger than at 8°. The two vortex structures remain distinct until approximately the 80% of the wing length; at this position the strake vortex (the inner vortex structure) is swallopped up by the stronger kink vortex. This last structure at the trailing edge strongly interacts with the tip vortex to give rise to a very complex structure. A possible interpretation of the oil flow visualisation at this incidence is reported on the right hand side of Figure 17; the vortical structures into two axial cutting planes are assumed following the topology rules but, unfortunately, this interpretation refers to a slightly greater incidence, namely 10.5°, performed during the more recent EPISTLE wind tunnel tests; therefore, it is not possible to make an exact comparison.

At the trailing edge, the inner vortex structure near the fuselage is not predicted by ZEN flow solver; this was the case also at 8°. The reason is due to the strake vortex which is not well "confined" close to the fuselage, i.e, the strake vortex tends to spread over the wing more than it actually occurs. Thus, the flow solver fails the prediction of the inner vortex structure at the trailing edge position. Nevertheless, the flow topology is qualitatively replicated at the outer wing.

4   Conclusions

The CIRA RANS flow solver ZEN has been successfully tested on the ESCT low-speed high-lift configuration. The goal was to demonstrate its capabilities to predict the global aerodynamic coefficients within the industrial accuracy requirements.

Four AOAs have been tested ranging from fully attached flow conditions (6°) up to partly separated flows (10°).

RANS equations have been solved with turbulent flow conditions both on the fuselage and the wing. The Kok TNT $\kappa - \omega$ turbulence model has been adopted for all computations. Some tests have been also performed with the Myong-Kasagi $\kappa - \epsilon$ turbulence model for comparison.

The convergence on the CIRA grid has been satisfactory and the global aerodynamic coefficients have reached a steady-state value at 6°, 8° and 9°. At 10°, the convergence has highlighted low-amplitude oscillations around a mean value.

- For the attached flow condition, the global aerodynamic coefficients are well within the accuracy requirements; the calculated pressure distribution highlights an excellent agreement with the experimental data and the limiting streamline plot replicates the experimental pattern.

- At 8°, the lift and the piching moment coefficient are well within the accuracy limits, while the drag value, when plotted against the lift, is just on the lower boundary of the acceptable band. The pressure distribution comparison is good except some discrepancies in the prediction of knuckle suction peak in the outboard wing section. The vortex structure close to the fuselage, mostly generated by the stub region, is not well captured. On the contrary, the kink vortex structure is well replicated in the simulation and dominates the flow development on the wing.

- By increasing the incidence, namely 10°, the onset of massive separated flow occurs; the lift and the pitching moment are well within the acceptance limits
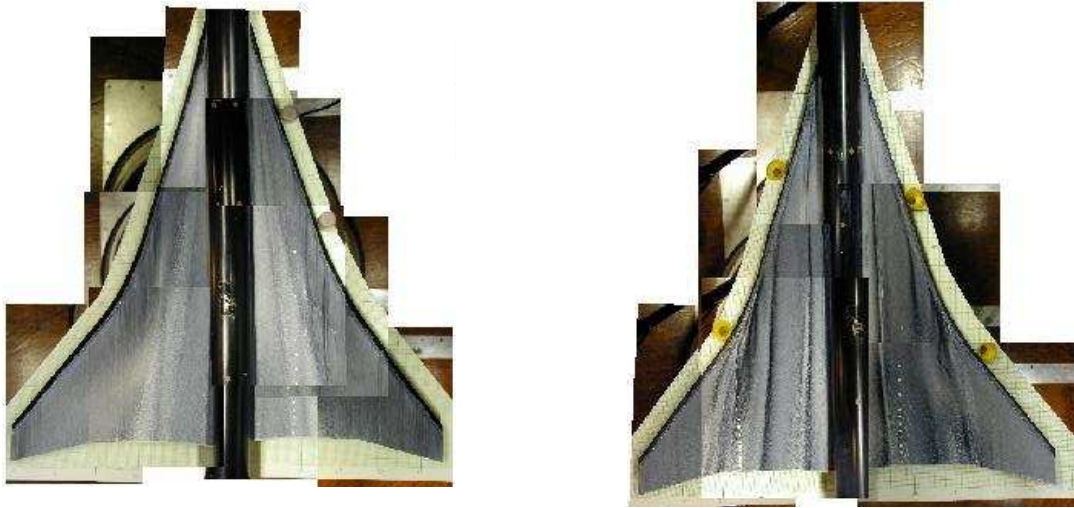
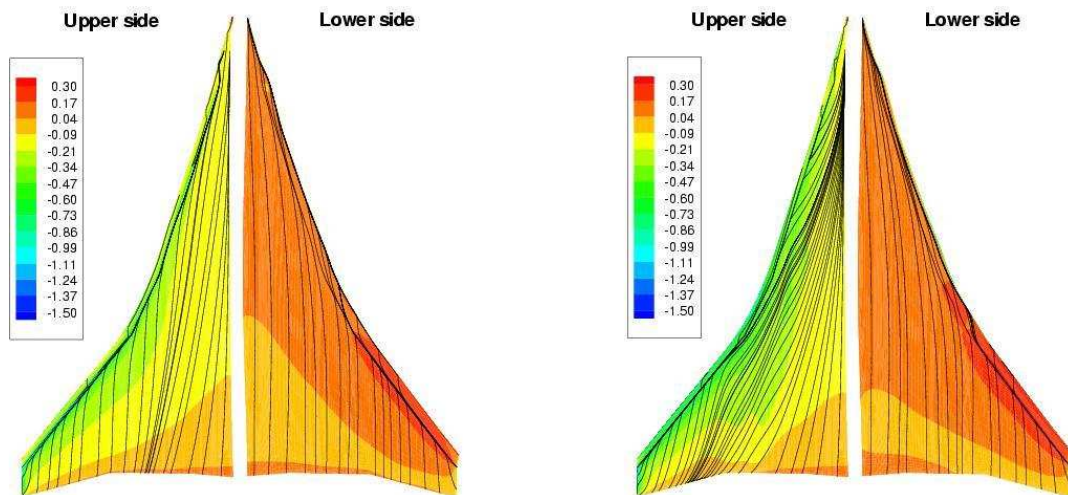**Fig. 13** Oil flow visualisation on the upper side of SCT wing, $\alpha = 6°$ (left) and $\alpha = 8°$ (right)

Fig. 14 Pressure coefficient contour plot with skin friction lines on lower and upper side, $\alpha = 6°$ (left) and $\alpha = 8°$ (right)

while the drag has been slightly overpredicted. Furthermore, the non-linearity of the experimental piching moment curve around the separation onset has been satisfactorily replicated. The pressure distribution is quite well predicted at the inner section with clear vortical flow downstream the hingeline position. A mismatch with the experimental data is evident in the mid-span and in the outboard section. The not accurate prediction of the vortical flow on the two external sections is mainly due to the circumstance that the simulation let the inner vortex spread over the wing more than it actually does.

The CIRA flow solver ZEN has predicted the ESCT aerodynamic performances within the industrial accuracy limits and the flow field behaviour has been satisfactorly captured.
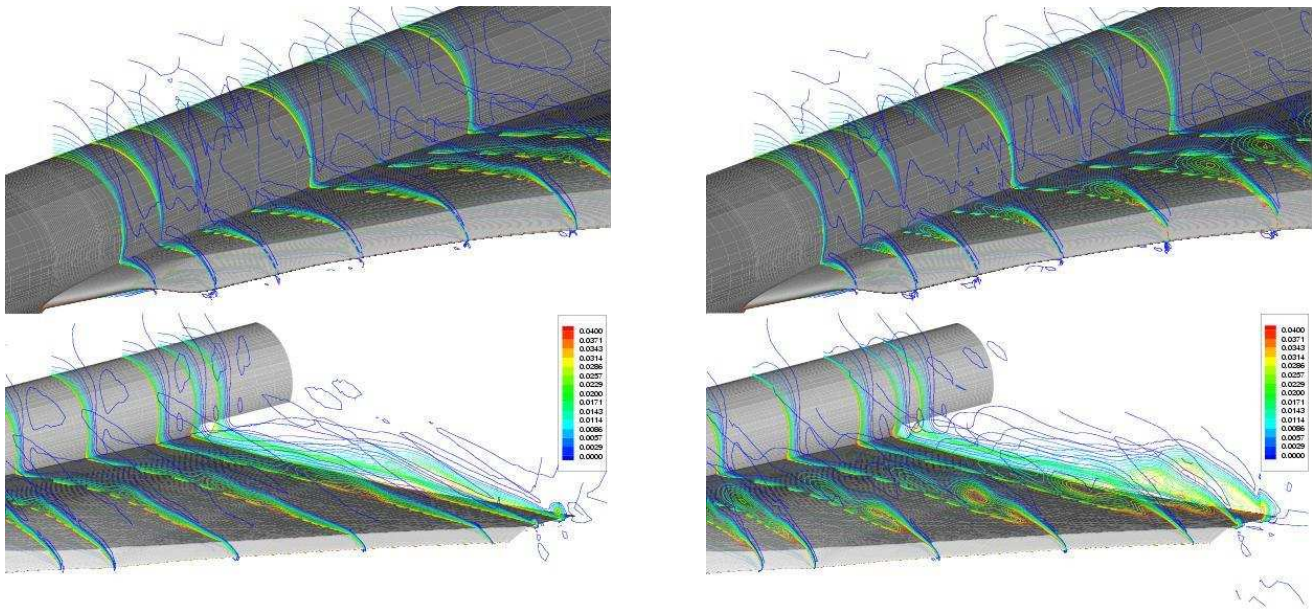
Fig. 15 Total pressure loss contour plot on axial cutting planes: top = detail of fore wing, bottom = detail of tip and trailing edge, $\alpha = 8°$ (left) and $\alpha = 10°$ (right)
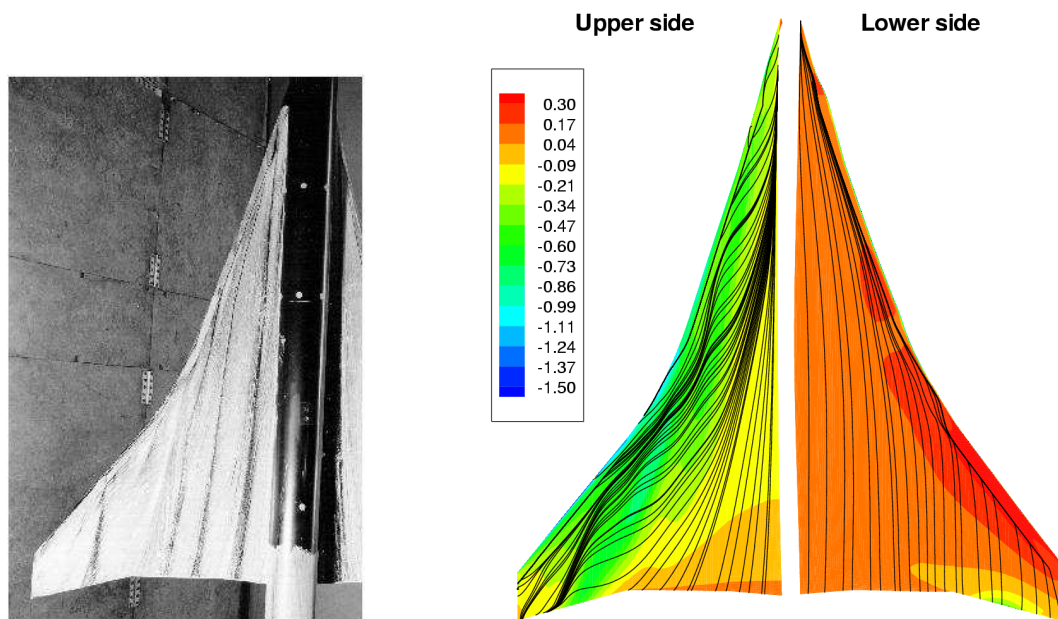

Fig. 16 Oil flow visualisation (left, from EUROSUP wind tunnel test campaign) and calculated pressure distribution with skin friction lines at 10°

References

[1] Brandi, V, Donelli, R S, Mingione, G. *Analysis of ESCT 1:80 model WT tests*, EPISTLE-13-CIRA-001, 2001

[2] Catalano P, Amato M. *Assessment of κ-ω turbulence modeling in the CIRA flow solver ZEN*, ECCOMAS CFD 2001 Conference, September 4-7 2001, Swansea, Wales, UK

[3] Elsenaar A. *Windtunnel Test of the EUROSUP SCT Configuration*, NLR-TR-98410, 1998 (also EUROSUP/NLR/T017/1).

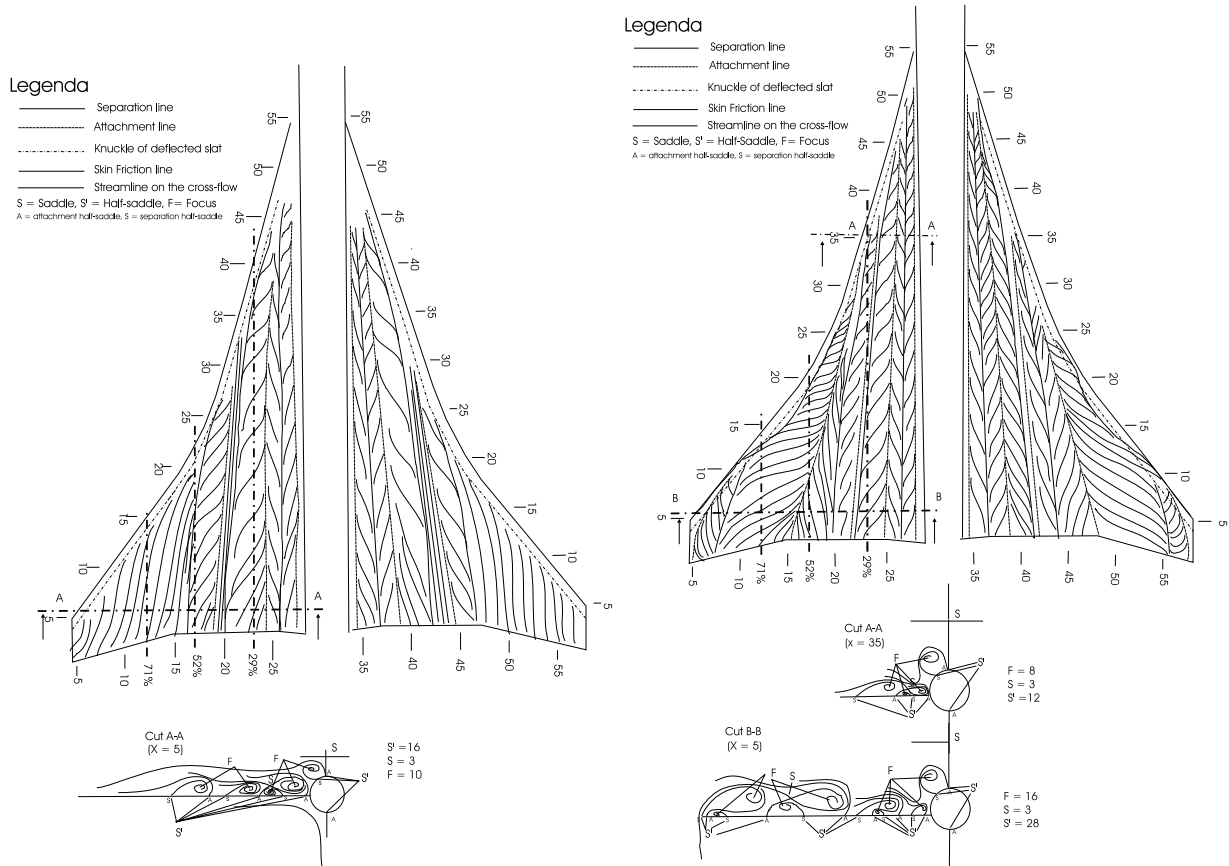[4] Elsenaar A. *EUROSUP Wind Tunnel test model specification*, NLR-TR-98287, 1998

Fig. 17 Topological interpretation of vortex flow on the upper side of SCT wing, $\alpha = 8°$ (left) and $\alpha = 10.5°$ (right, both from reference [1])

(also EUROSUP/NLR/T010/3).

[5] Herrmann, U et alii. *Validation of European CFD Code for SCT low-speed high-lift Computations*, AIAA Paper 2001-2405, 19th Applied Aerodynamics Conference, June, 11-14 2001, Anaheim, USA

[6] Kok J C. *Resolving the dependence on freestream values for the κ-ω turbulence model*, AIAA Journal, Vol. 38, n. 7, July 2000, pp. 1292-1295

[7] Kok J C, Amato M, Boerstoel J W. *Mathematical-Physical modeling for multi-block NaS/Euler simulation*, CIRA-DLCEST-TR183, and NLR-CR91-235L

[8] Lowell D A. *European research of wave and lift dependent dragfor supersonic transport aircraft*, AIAA Paper No. 99-3100, 1999

[9] Myong H, Kasagi N. *A new approach to the improvement of the $\kappa - \varepsilon$ turbulence model for wall bounded shear flow*, JSME Intern.

J., serie 2, 33, N. 1. pp. 63-72

[10] Rohne P B. *Data Report of Wind Tunnel measurements on the EUROSUP model*, NLR-CR-98495 also EUROSUP/NLR/T018/1.

[11] Rohne P B. Hoolhorst A and Goossens J D. *Data Report on Low Speed Measurements in the HST for the EPISTLE Project*, DNW-ASD-2000-032, 2000 (also EPISTLE-12-NLR-002)